LIGHTCURVE INVERSION FOR SHAPE ESTIMATION OF GEO OBJECTS FROM SPACE-BASED SENSORS

Ben K. Bradley[(1)] **and Penina Axelrad**[(2)]

[(1)(2)]*University of Colorado Boulder, UCB 431, ECNT 320, Boulder, CO 80309, USA,*
ben.bradley@colorado.edu

Abstract: *Shape estimation is one of the key aspects of recent space situational awareness (SSA) research efforts. Much SSA work is focused on characterizing space objects through estimation of attitude, rotation rate, area/shape, and then to extrapolate object type, mission, and operational status. This paper presents an initial investigation of using photometric data with a lightcurve inversion technique commonly used for asteroid shape estimation, to approximate the shape of man-made objects in the geosynchronous belt (GEO). Specifically, this paper uses simulated photometric observations of a an upper stage rocket body, a high area-to-mass ratio (HAMR) object, 1U and 3U CubeSats, as well as a box-wing satellite taken from a space-based optical sensor to assess the feasibility of this lightcurve inversion method. Results indicate it is a beneficial technique for rocket bodies and CubeSats, while showing only moderate difficulties with HAMR objects and box-wing shapes. Suggestions for algorithm improvements and future work are included.*

Keywords: *Lightcurve Inversion, Shape Estimation, Space Surveillance, Orbital Debris.*

1. Introduction

The growing catalog of both satellites and debris alike motivates the space community to improve orbit determination and propagation of these objects to prevent future collisions. In part, these improvements are aided by better knowledge of what each object actually is; its shape, mass, operational status, etc. While some of this information may not directly aid in avoiding collisions, it does help identify threats and improve our overall knowledge of the objects that occupy the space around Earth. The shape of these resident space objects (RSOs) is of particular interest, because it allows for the inference of size, mass, and possibly operational status. Furthermore, objects in the geosynchronous (GEO) belt are of specific concern because this unique region is such a valuable, limited resource. The intent of this paper is to evaluate the feasibility of using lightcurve inversion (LCI) to estimate the shapes of typical geosynchronous and near-geosynchronous objects (e.g., rocket bodies and satellites), both active and inactive.

The use of photometric measurements for estimating size and shape has become popular in both the space situational awareness (SSA) community [1–4] and the asteroid community [5, 6] over the last decade or so. Thus far, LCI has been proven to be a valuable tool to this end. The LCI technique developed by Mikko Kaasalainen and Johanna Torppa has been instrumental to the asteroid community for generating shapes of countless asteroids [7, 8]. There have been a few studies that investigated the use of LCI and related techniques on satellites, but they have assumed known attitude states, only used random polyhedron or cube-shaped objects, and only simulated photometric measurements from ground-based telescopes [9–12]. Other studies in the SSA community have used various Kalman filters, including the use of multiple-model adaptive estimation (MMAE), to estimate polyhedron and cube-shaped objects as well as attitude [3, 13, 14].

While these methods look promising, they focus on "debris-shaped objects instead of typical satellite shapes.

The contribution of our research is the application of LCI based on photometric measurements from space-based sensors to object types commonly found in GEO. Space-based space surveillance (SBSS) is required to observe GEO objects without weather restriction and with improved viewing geometry. With the recent launches of SBSS satellites such as SBSS Block 10[1], Sapphire, NEOSSat, and STARE [15–17], this study will help to determine if LCI is a feasible option for utilizing the photometric measurements being produced. Simulated photometric measurements from a space-based optical platform in Sun-synchronous orbit are used to estimate convex shape models and rotation poles of an upper stage rocket body, a high area-to-mass ratio (HAMR) object, 1U and 3U CubeSats, as well as a box-wing satellite. This feasibility study seeks to assess the challenges and limitations of LCI in working with each of these objects.

2. Lightcurve Inversion Process

2.1. Lightcurve Model

This section outlines the computation of lightcurves as well as the inversion process. We start with computing the brightness of the target object at a given moment in time. This requires the object's shape (consisting of a finite number of flat plates), attitude, and position as well as the location of the observer and the Sun. At the time of an observation, let us define unit vectors from the target to the observer ($\mathbf{u}_{obs}^B$) and from the target to the Sun ($\mathbf{u}_{sun}^B$), both expressed in the body frame of the target. Superscripts of vectors are either B or I, indicating that the vector is defined in the body or inertial frame, respectively. The total brightness of the target object, made up of n facets, as seen by the observer is given by

$$L = \sum_{j=1}^{n} S(\mu, \mu_0, \alpha) \, \rho_j \, a_j, \tag{1}$$

where S is the scattering law (or bidirectional reflectance distribution function, BRDF), ρ_j is the albedo of the j-th facet, a_j is the area of the j-th facet, and α is the solar phase angle. The BRDF model determines the way in which light is reflected off of each plate. Each facet has a surface area, albedo, and surface normal vector, which completely define the shape's reflectance properties. The parameters μ and μ_0 are equal to the dot product of the facet normal vector $\mathbf{u}_n^B$ with $\mathbf{u}_{obs}^B$ and $\mathbf{u}_{sun}^B$, respectively. The solar phase angle (α) is the observer-target-Sun angle, defined by $\arccos(\mathbf{u}_{obs}^I \cdot \mathbf{u}_{sun}^I)$. This can be computed using vectors either in the inertial frame or body frame.

Specifically, Eq. 1 yields a "calibrated" brightness value, in which the target-observer distance and power from the Sun are not used. This effectively reduces the target-observer distance to a unit distance. This definition of brightness is used in Ref. 5 as well as by the LCI software suite discussed in Sect. 2.3.

---

[1]http://www.afspc.af.mil/library/factsheets/factsheet.asp?id=20523

As previously mentioned, the BRDF determines how light is reflected off of an object. The BRDF used for this paper is a combination of Lommel-Seeliger (S_{LS}) and Lambert (S_{L}) laws [5, 18]. This particular combination works well for modeling asteroids and extrasolar planets and is currently used by the LCI software suite [5, 6]. The BRDF is constructed as

$$
\begin{aligned}
S(\mu, \mu_0, \alpha) &= f(\alpha) \left[S_{\mathrm{LS}}(\mu, \mu_0) + c S_{\mathrm{L}}(\mu, \mu_0) \right] \\
&= f(\alpha) \mu \mu_0 \left(\frac{1}{\mu + \mu_0} + c \right),
\end{aligned}
\tag{2}
$$

where $f(\alpha)$ is the phase function

$$
f(\alpha) = A_0 \exp \left(-\frac{\alpha}{D} \right) + k\alpha + 1.
\tag{3}
$$

The parameter c is a weighting factor that determines the contribution of the Lambert scattering law. The phase function is determined by the amplitude and scale length of the opposition effect (A_0 and D) as well as the slope of the phase curve (k). The simulations presented in this paper use the baseline recommended values given by Ref. 6 and are left as fixed parameters during the shape and rotation pole estimation process ($c = 0.1$, $A_0 = 0.5$, $D = 0.1°$, $k = -0.5$).

In the SSA and computer graphics communities, two other BRDF models known as Ashikhmin-Shirley and Cook-Torrance have been in common use in recent years [19–22]. They have the advantage of being fast empirical models which incorporate both diffuse and specular reflections. These models are likely to represent typical spacecraft materials more accurately than the Lommel-Seeliger/Lambert scattering law, however, this initial investigation seeks to determine how LCI handles man-made type shapes and not to be the final verdict on shape estimation accuracy. Implementing a model such as Ashikhmin-Shirley with LCI is planned for future work.

2.2. Lightcurve Inversion

This section briefly outlines the process of lightcurve inversion as laid out in Ref. 5 and 6. Essentially, the inversion for convex shapes can be written as

$$
\boldsymbol{L} = A\mathbf{g},
\tag{4}
$$

where $\boldsymbol{L}$ is the complete set of brightness measurements taken of the target, A is a matrix consisting of the BRDF and albedo values, and $\mathbf{g}$ is a vector consisting of the facet areas to be solved for. We have

$$
A_{ij} = S(\mu_{ij}, \mu_{0,ij}, \alpha_i)\rho_j, \quad j = 1, 2, \ldots, n, \ \ i = 1, 2, \ldots, N,
\tag{5}
$$

where j identifies the facet and i identifies the observation number. The vector $\mathbf{g}$ is constructed such that

$$
g_j = \exp(a_j).
\tag{6}
$$

The exponential of the facet areas is used in place of just area in order to eliminate the need for manually constraining or using barrier functions to ensure that each facet area is positive. Moving

3

back to Eq. 4, the solution to this problem is found by minimizing

$$\chi^2 = \|\boldsymbol{L} - A\mathbf{g}\|^2, \tag{7}$$

by using the conjugate gradient method [5]. Other methods may require *a priori* information about the shape, which is usually not attainable. The LCI algorithm implemented in the software actually uses a normalized form

$$\chi^2 = \sum_{k=1}^{M} \left\| \frac{\boldsymbol{L}^{(k)} - A^{(k)}\mathbf{g}}{\bar{L}^{(k)}} \right\|^2, \tag{8}$$

where k identifies each observation pass and $L^{(k)}$ is the mean brightness of the k-th pass. This normalized form gives each observing geometry equal weights. Once the facet areas are solved for, Minkowski minimization is used to solve for the vertices of each facet so that a 3D model can be generated [5].

Once a shape model and rotation pole have been solved for, brightness measurements may be computed and compared with the original observations. The simulation results presented in this paper display a root-mean-square (RMS) value of the relative χ^2 error denoted

$$\chi_{\text{RMS}}^2 = \sqrt{\chi_{\text{rel}}^2 / N}, \tag{9}$$

where

$$\chi_{\text{rel}}^2 = \sum_{k=1}^{M} \left\| \frac{\boldsymbol{L}_{\text{obs}}^{(k)}}{\bar{L}_{\text{obs}}^{(k)}} - \frac{\boldsymbol{L}^{(k)}}{\bar{L}^{(k)}} \right\|^2. \tag{10}$$

Here, we have the observed $\boldsymbol{L}_{\text{obs}}^{(k)}$ and modeled $\boldsymbol{L}^{(k)}$ lightcurves and their respective mean brightness values $\bar{L}_{\text{obs}}^{(k)}$ and $\bar{L}^{(k)}$.

When Eq. 8 is used, the relative structure of the lightcurve is matched and not necessarily the absolute values of the brightness measurements. This usually results in a slight scaling error in which the lightcurve behavior of the LCI solution shape matches the normalized observed lightcurves, but their actual values are either too large or too small. To alleviate this problem, we essentially want to minimize

$$\|\boldsymbol{L} - c_{\text{scale}}\boldsymbol{L}_{\text{LCI}}\|, \tag{11}$$

where c_{scale} is some scaling factor. This is easily computed by

$$c_{\text{scale}} = \frac{\sum_{i=1}^{N} L_{\text{obs}}^{(i)} L^{(i)}}{\sum_{i=1}^{N} L^{(i)2}}. \tag{12}$$

Given the facet areas solved for by the LCI procedure, the improved solution can be obtained by performing $a_j c_{\text{scale}}$ to yield the new facet areas. If Minkowski minimization has already been performed to compute the facet vertices, the coordinates of each vertex should be multiplied by $\sqrt{c_{\text{scale}}}$ to achieve the properly scaled 3D shape model. Refer to Ref. 5 and 6 for more details on either the scattering model or LCI algorithm.

2.3. Software

Results presented in this paper were generated using the LCI software suite made publicly available by Mikko Kaasalainen and Josef Ďurech through the Database of Asteroid Models from Inversion Techniques (DAMIT) website.[2] Specifically, version 0.2.1 of the LCI software was used in this study. This is a professional implementation of the LCI algorithm presented in Ref. 5, which has been converted from Kaasalainen's original Fortran code to C by Josef Ďurech. A MATLAB program was written to compute brightness measurements of desired shapes and then interface with the LCI C-code to estimate the object's shape and rotation pole.

3. Shape Model Definition and Simulation Setup

3.1. Rotation Description

The simulated objects modeled in this study each rotate with the same period and pole direction. This maintains similar observation conditions for each object so that there is no advantage or disadvantage given to any particular simulation. The pole direction of the target body is described by the inertial polar angle $\tilde{\beta}$ and right ascension λ. The inertial coordinate system used is the Geocentric Celestial Reference Frame (GCRF) since the targets are in Earth orbit. Studies involving asteroids may choose to refer to the ecliptic instead, as is done in Ref. 6. The polar angle is measured positive from the z axis. Therefore, the latitude of the pole is defined as $\beta = 90° - \tilde{\beta}$. The 3-2-3 Euler rotation

$$\mathbf{r}_B = R_z(\phi_0 + \omega(t - t_0))R_y(\tilde{\beta})R_z(\lambda)\mathbf{r}_I, \tag{13}$$

transforms a position vector expressed in the inertial frame into the body frame of the target where ω is the rotation rate of the target body. The epoch time t_0 and rotation angle ϕ_0 may be chosen by the observer, either by some predefined convention or simply zero degrees at the time of the first observation. The rotation matrices R_γ correspond to conventional frame rotations about the corresponding γ axis.

The following simulations consist of target objects with a rotation pole of $\beta = 30°$ and $\lambda = 97°$. In each case the two pole parameters are given an incorrect *a priori* guess and are then estimated through the LCI process. The rotation period of each object is 2 minutes and is held fixed. A 2-minute period is a reasonable approximation for defunct GEO objects and upper stage rocket bodies, based on observations and analytic studies to date [23–25].

3.2. Simulation Overview

Each simulation consists of a space-based optical sensor in a Sun-synchronous orbit taking brightness measurements of a target object in GEO. The sensor orbit has an inclination of 99.024° and is aligned near the dusk-dawn terminator. Each target in GEO is inclined at 2° to the equator and has a semi-major axis of 42,170 km. Brightness measurements are taken in groups of 25 with 25-second spacing over the course of 80 days. Figure 1(a) depicts the phase angle of each measurement,

---

[2]DAMIT Website: `http://astro.troja.mff.cuni.cz/projects/asteroids3D/web.php`

demonstrating the wide range of values and their sparsity. The observation schedule essentially consists of a few patches of observations in one day and then a gap of 11.6 days. This pattern then repeats for the duration of 80 days to ensure that the observations span a large range of phase angles and changing Sun positions.
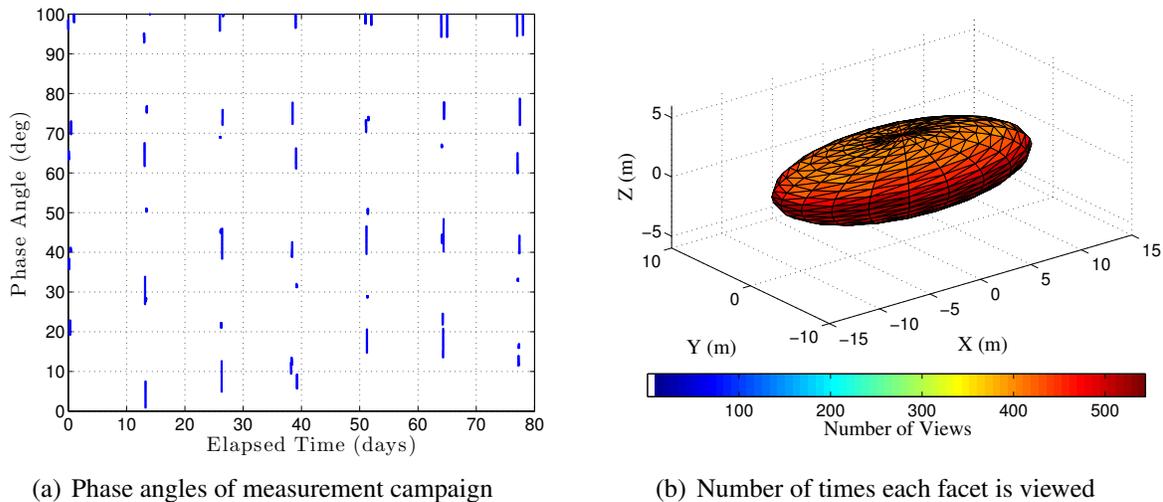

(a) Phase angles of measurement campaign (b) Number of times each facet is viewed

Figure 1: Observations used in simulation.

We present LCI results for several shapes, including a simple ellipsoid test case, Centaur upper stage, 1U and 3U CubeSats, HAMR object, and a box-wing satellite. Each shape consists of triangular facets defined by their surface normal vectors and surface area. The truth light curves are not generated with self-shadowing taken into account, unless otherwise noted. For simulations that do incorporate self-shadowing, a simple ray tracing algorithm was used to determine shadows, but not secondary reflections [26]. Figure 1(b) illustrates the number of times each facet of a general ellipsoid is viewed during the simulated observation campaign. This figure illustrates that the entirety of the object is viewed and with nearly an equal distribution of observations.

4. Simulation Results

This section discusses the simulation results for each shape mentioned previously. The LCI process estimates the object's shape as well as pole direction defined by λ and β. For each object, the true shape is displayed next to the shape recovered from LCI for a visual comparison. We report the χ^2_{RMS} value for all simulations and plot lightcurves from two different viewing geometries over a full $360°$ rotation of the object, as is done in Ref. 5 and 6. This creates a more comprehensive lightcurve comparison that encompasses the entire body instead of snapshots from the original measurement set.

Table 1 summarizes the pole estimates and lightcurve χ^2_{RMS} errors for each shape and for several different *a priori* pole values. Each case will be discussed in detail in the following sections, but we give a summary here for convenience. Table 1 illustrates that the rotation poles of the ellipsoid, Centaur upper stage, and 3U CubeSat are capable of being accurately recovered by LCI when given large initial errors. The 1U CubeSat is also able to recover from a moderate initial error. In contrast,

LCI does not settle on the correct pole for the HAMR and box-wing objects, even when the initial error is quite small. For these two objects, we also present a case where the pole is held fixed at the correct value (indicated by an "NA" in the 3rd column) to yield insight into the shape estimation.

Table 1: Pole estimates and RMS lightcurve errors for each shape. The true pole direction is $\lambda = 97°$ and $\beta = 30°$. An entry of "NA" in the estimated pole field indicates that the initial values given for the pole were held fixed and not estimated.

Object	A Priori λ, β	Estimated λ, β	χ^2_{RMS}
Ellipsoid	120, 0	96.9, 30.6	0.0085
Centaur	120, 0	97.0, 30.0	0.0238
1U CubeSat	120, 0	141.9, 7.1	0.1164
1U CubeSat	90, 20	97.2, 29.8	0.0263
3U CubeSat	120, 0	97.1, 29.5	0.0285
HAMR	120, 0	125.7, 1.6	0.1993
HAMR	97, 30	NA	0.1031
Box-Wing	97, 30	NA	0.0806
Box-Wing	95, 28	93.6, 12.1	0.1018

4.1. Test Case: Ellipsoid

A basic ellipsoid is used as our test case to demonstrate a working algorithm. The strong convexity of this ellipsoid is a very natural asteroid-like shape for the LCI algorithm to work with. Table 1 shows that the pole is estimated to within 1° when given a large initial error. Figure 2 illustrates the larger size of the LCI estimated shape as compared to the true shape, but still yields a lightcurve that is very similar to the original. The lightcurves generated from two different viewing geometries (one with a large phase angle of 95° and one at 15°) shown in Fig. 3 are again quite similar. Note that this is by far the easiest type of shape for LCI to estimate because there are no concavities or bulges. The following sections investigate more challenging shapes that are prevalent in and near the GEO belt.
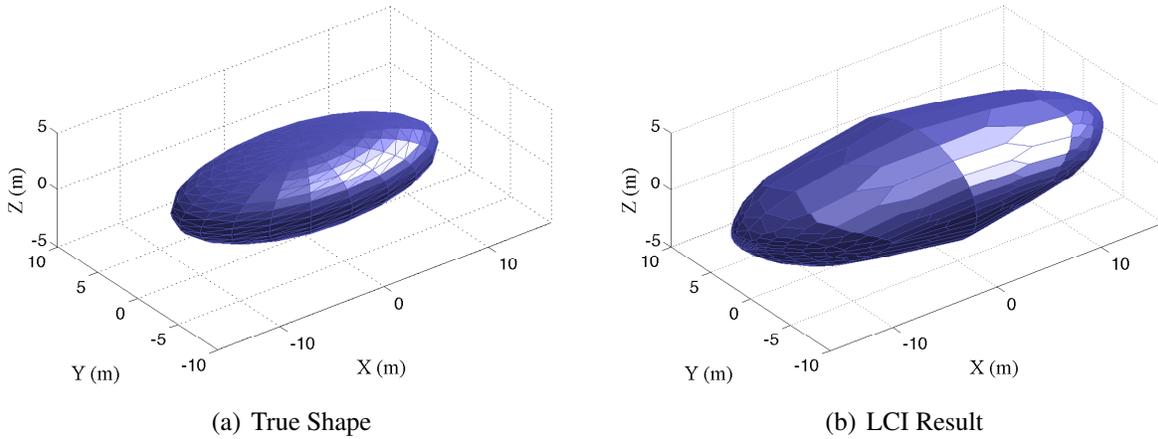
(a) True Shape

(b) LCI Result

Figure 2: Truth and LCI shape models in body frame for the test ellipsoid.

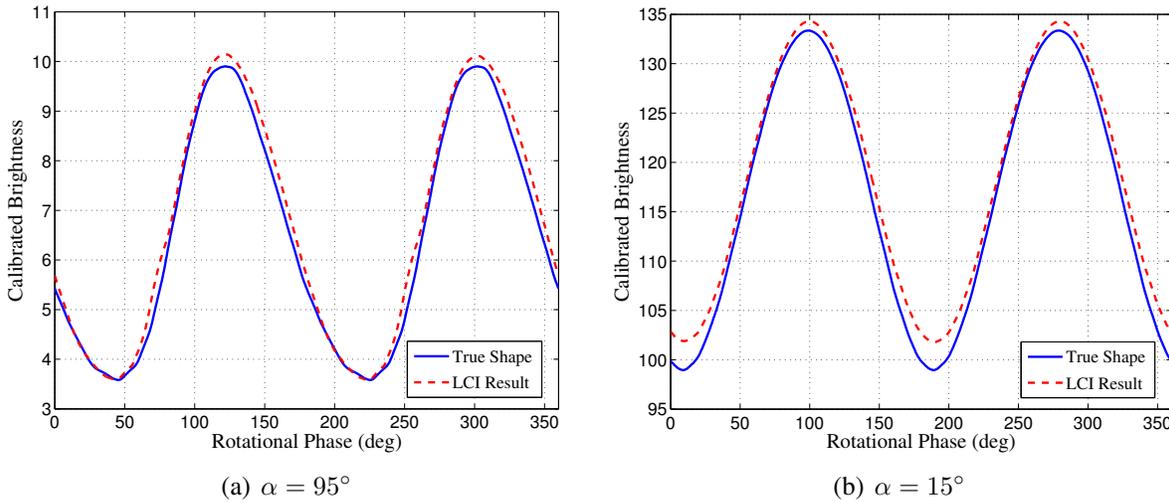(a) $\alpha = 95°$

(b) $\alpha = 15°$

Figure 3: Lightcurve comparisons for two different viewing geometries of the test ellipsoid.

4.2. Upper Stage Rocket Body: Centaur

In order to deliver a spacecraft to the GEO belt, an upper stage rocket engine is used to first place the spacecraft into a geostationary transfer orbit (GTO). Common upper stage rocket bodies include the Centaur (part of the Atlas V launch system), the ESC-A (part of the Ariane launch system), and the Falcon 9 upper stage from SpaceX. This section focuses on the Centaur, but most upper stages have similar geometry, consisting of a main cylinder for fuel storage and a rocket nozzle. Upper stages are typically left in GTO trajectories with low perigee altitudes in order to adhere to the 25-year deorbit guidelines. However, they still spend several years in GTO before reentering Earth's atmosphere.

The Centaur shape used for truth is depicted in Fig. 4(a). The shape consists of a main cylindrical tank with rounded caps and a parabolic nozzle. The smaller features such as tubing and small

spherical tanks near the nozzle have been omitted for simplicity. The resulting shape from LCI in Fig. 4(b) mimics the cylinder quite well, although we note that it is a few meters shorter than the actual Centaur model. This is likely due to the difficulty in generating a straight cylinder. Since the LCI technique wants to create a convex shape, it clearly gives the modeled cylinder a slight bow in the midsection. This bow yields more light being reflected in certain directions, thus compensating for the shorter body. The backside of the LCI shape solution, Fig. 5, is marked with a large red facet, denoting the dark facet area. Recall that the dark facet is one that makes the overall shape model formally convex, but it not intended to contribute photometrically. In most cases, it is desirable to limit the area of the dark facet to below 1%, as recommended by Ref. 5. However, the backside of the truth Centaur model contains the nozzle which reflects light in varying directions and has a dark interior. Thus, LCI simply does not model the backside. Even with this large dark facet, Fig. 6 demonstrates that the LCI shape captures the subtle features of the true lightcurve quite well. The rotation pole of the upper stage is also estimated quite easily as shown in Tab. 1. This method of LCI, at the very least, could indicate that the target body is an upper stage with a particular spin axis. With this *a priori* information, other methods such as multiple model adaptive estimation (MMAE) could be used to determine the exact upper stage model.
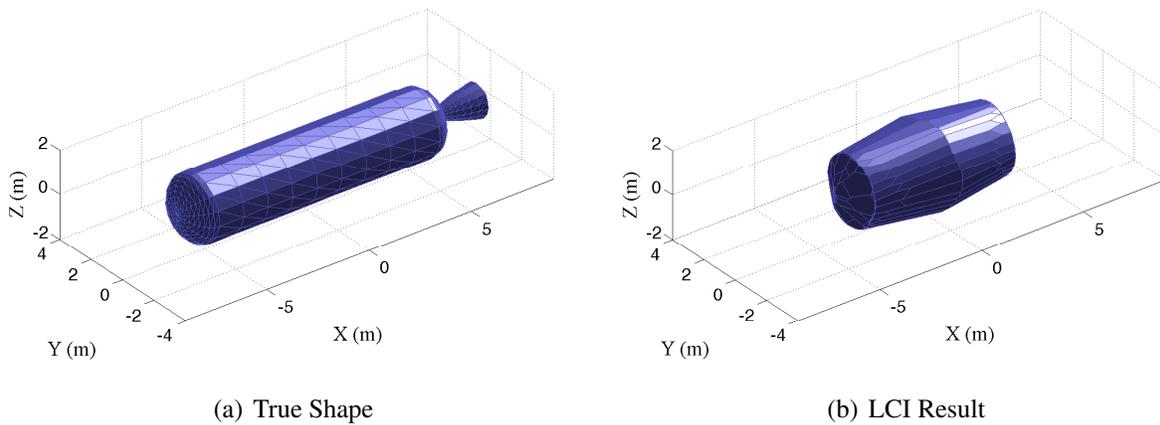

(a) True Shape   (b) LCI Result

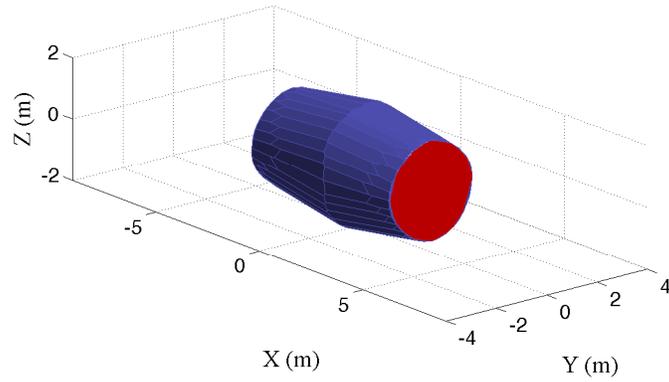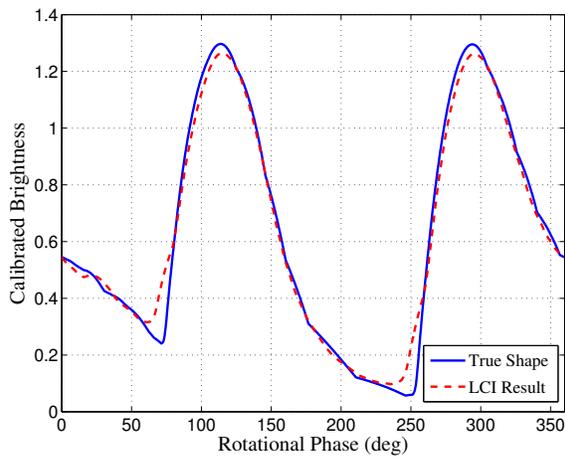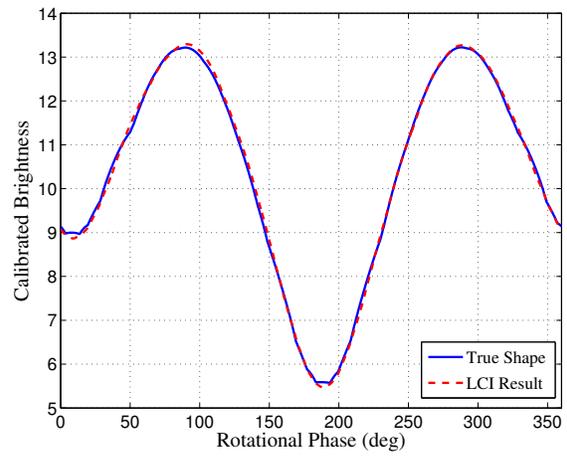**Figure 4: Truth and LCI shape models for the Centaur upper stage.**

9

Figure 5: Backside of the LCI shape solution for the Centaur.

(a) $\alpha = 95°$

(b) $\alpha = 15°$

Figure 6: Lightcurve comparisons for two different viewing geometries of the Centaur upper stage.

4.3. 1U CubeSat

This section investigates shape and pole recovery of a 1U CubeSat in the GEO belt. In reality we model the 1U CubeSat as a square box with 1-meter sides instead of the typical 0.1-meter sides of an actual CubeSat. This is done simply to increase the brightness return from the target object. The use of CubeSats, whether they be 1U or 3U configurations, is increasing as their capabilities are expanded. They most commonly reside in LEO, however, they may be used in GEO in the near future [27].

Figure 7 demonstrates that LCI can be used effectively to recover a cube. There are a few items to note, however. First, the recovered cube has a side length of approximately half of the true cube. The LCI recovered cube does not possess perfectly flat plates as illustrated in Fig. 7(b). Instead, each side has a slight peak where 4 separate facets come together. As with the Centaur rocket body, the angles plates reflect more light in certain directions to compensate for the smaller overall size of the object. As a result, the lightcurves of each shape match quite well as seen in Fig. 8. The box-looking LCI solution would be enough information to conclude that the target object is likely a 1U CubeSat.

The second item to note is that the initial rotation pole guess must be closer to the true pole than was previously demonstrated by the ellipsoid and the upper stage. Table 1 shows that we are able to recover from an incorrect initial estimate, but a smaller one than previously used. A large initial pole error causes LCI to settle on an incorrect pole value and a shape to go along with it. Figure 9 depicts an octahedron resulting from an incorrect pole solution. One possible approach, mentioned in Ref. 6, is to run LCI multiple times with different initial rotation pole estimates. The solution with the lowest χ^2_{RMS} value is likely the best estimate for pole and shape.
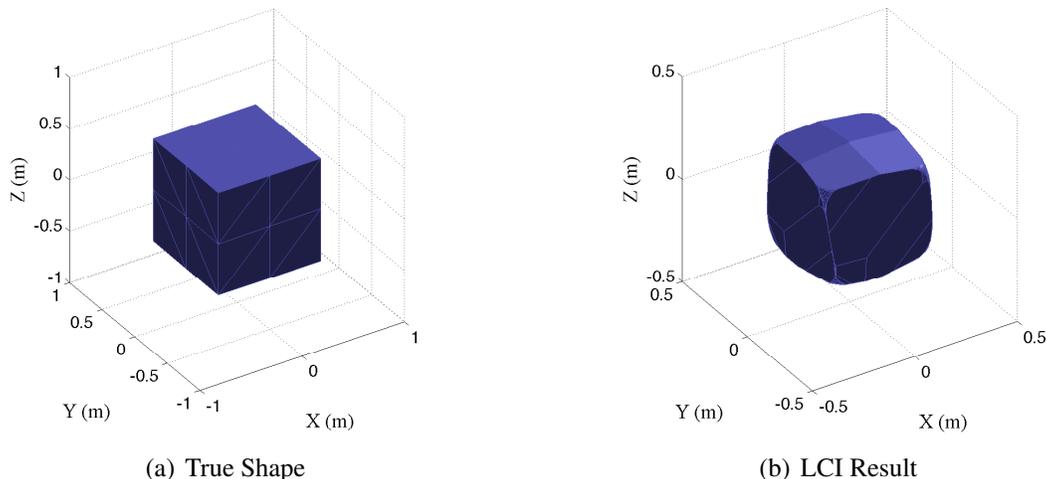

(a) True Shape   (b) LCI Result

Figure 7: Truth and LCI shape models for a 1U CubeSat.
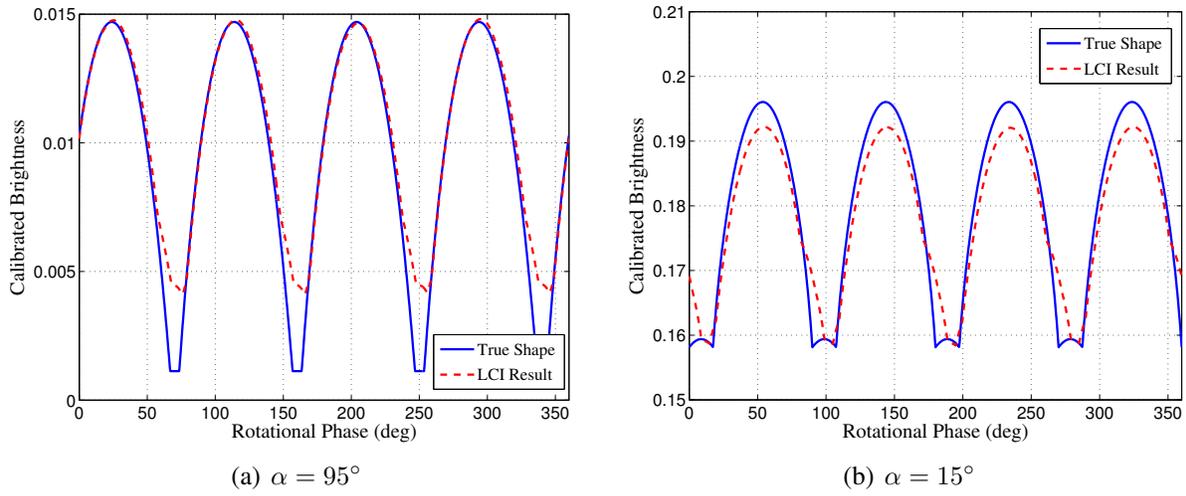
11

(a) $\alpha = 95°$

(b) $\alpha = 15°$

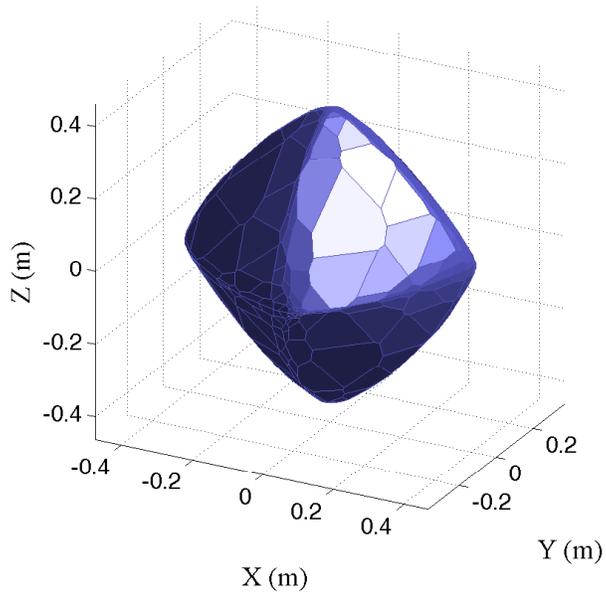**Figure 8: Lightcurve comparisons for two different viewing geometries of the 1U CubeSat.**

Figure 9: LCI shape solution for a 1U CubeSat when settled on an incorrect rotation pole. The shape is similar to an octahedron.

4.4. 3U CubeSat

As was done with the 1U CubeSat, we have increased the size of the 3U CubeSat model to 1m x 1m x 3m, as shown in Fig. 10(a). Figures 10 and 11 depict results for the LCI estimated shape and lightcurve comparisons when the *a priori* pole estimate has a large error, $\lambda = 120°$ and $\beta = 0°$. Recall that the true pole is $\lambda = 97°$ and $\beta = 30°$. While the 1U CubeSat required a moderately close initial guess, the pole of the 3U CubeSat is able to be accurately solved for when given this large initial error.

(a) True Shape
(b) LCI Result

Figure 10: Truth and LCI shape models for a 3U CubeSat.

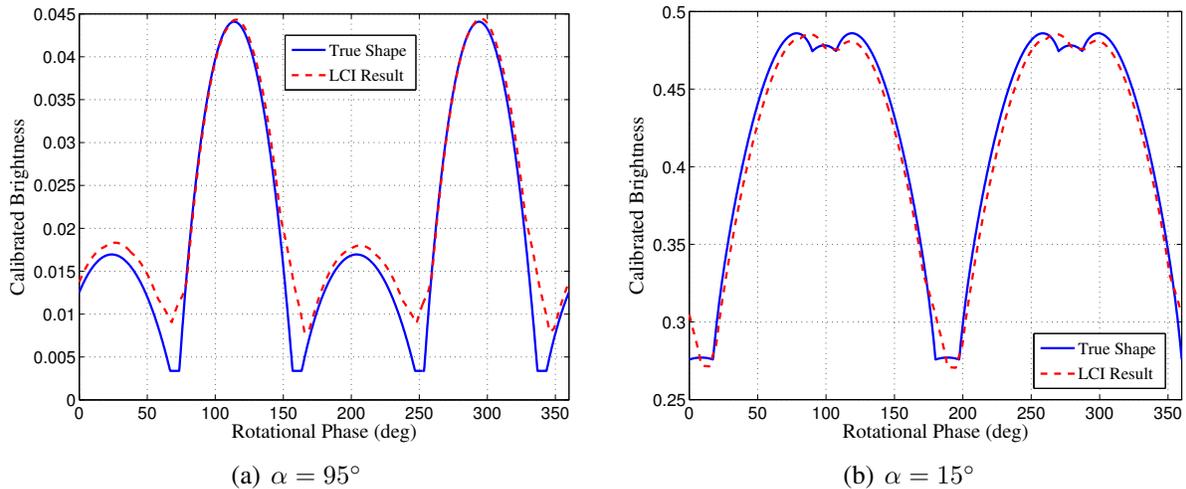(a) $\alpha = 95°$
(b) $\alpha = 15°$

Figure 11: Lightcurve comparisons for two different viewing geometries of the 3U CubeSat.

13

4.5. HAMR Object

High area-to-mass ratio (HAMR) objects have only recently been detected in near-GEO orbits and are thought to be sheets of multi-layer insulation (MLI) that have detached from GEO satellites [28, 29]. This type of object is difficult to reliably propagate and track due to the increased influence of solar radiation pressure (SRP) and thus the attitude of the MLI. Recent studies have sought to better understand the long-term motion of these HAMR objects by performing detailed 6 degree-of-freedom simulations [30, 31]. These studies conclude that SRP torques cause the attitude and rotation axis of HAMR objects to change slowly over time.

This section seeks to determine if LCI, in its current form, is capable of recovering the shape of flat plates and their rotation pole. Note that a flat plate is a commonly used shape to approximate a HAMR object since they are thought to be sheets of MLI. Unfortunately, a rigid flat plate, as shown in Fig. 12(a), is difficult for LCI to estimate the shape and rotation pole for. When given an incorrect rotation pole as an *a priori* guess, LCI settles on an incorrect pole and shape. Even when the initial pole estimate is the true pole, if the pole parameters are left as free parameters, LCI diverges from the true pole values. Figure 12(b) depicts the LCI shape solution when the correct pole is given and held fixed. In this case, the inversion process is able to yield a reasonable approximation to a flat plate, a thin circular disc. This makes intuitive sense, because the the square plate is spinning.
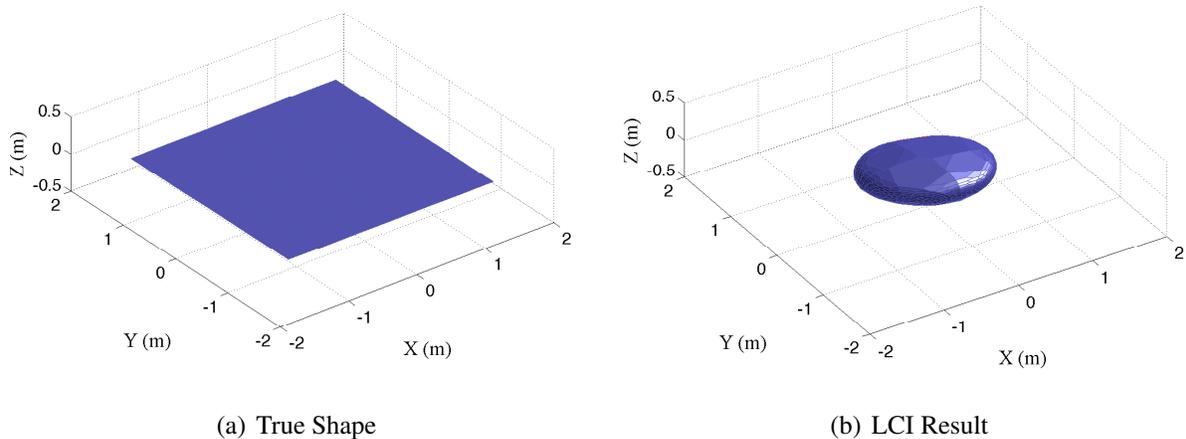

(a) True Shape

(b) LCI Result

Figure 12: Truth and LCI shape models for the flat plate HAMR object. LCI shape solution generated with the true rotation pole.
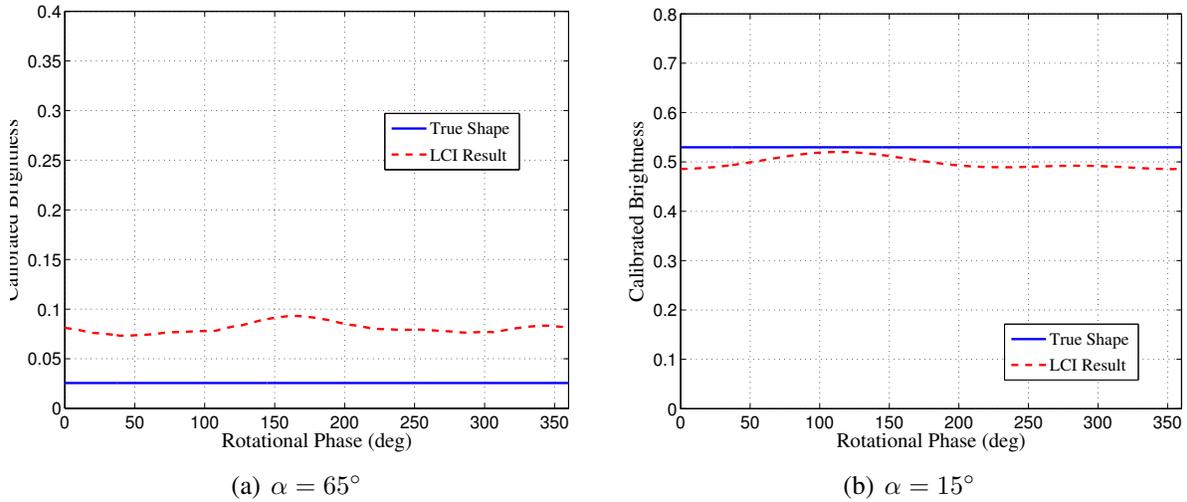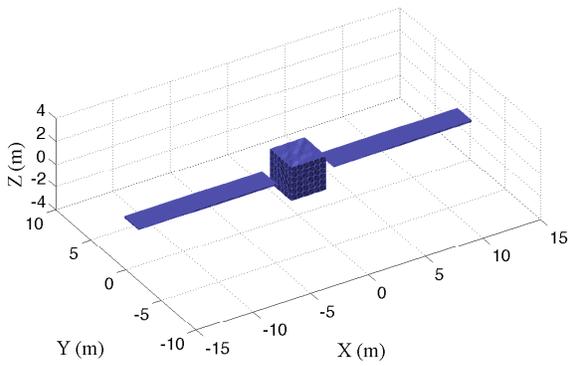
(a) $\alpha = 65°$
(b) $\alpha = 15°$

Figure 13: Lightcurve comparisons for two different viewing geometries of the flat plate HAMR object. The LCI solution is based on the thin disc generated using the true rotation pole.
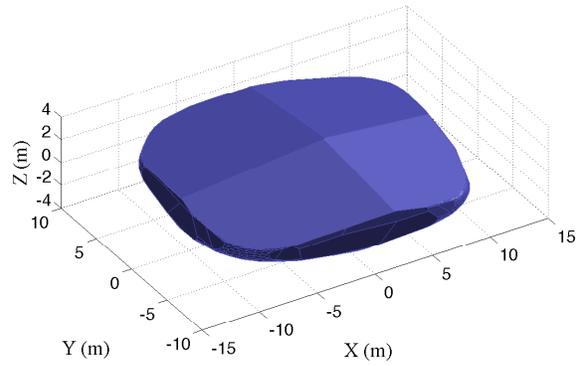
4.6. Box-Wing Satellite

We conclude with a geostationary satellite modeled using a box-wing configuration. A box-wing design is a reasonable approximation for many GEO satellites which usually contain a square or rectangular main bus and large solar panels on each side. The true shape, shown in Fig. 14(a), models the main square bus using ruffled plates (i.e., not perfectly flat) in an attempt to approximate a crinkled MLI covering. Additionally, the solar panels are given a thickness of 12 cm. Since the rotation period is left at 2 minutes and the box-wing rotates about the body z axis as depicted below, this simulation mimics a defunct and drifting satellite in the GEO belt.

As with the HAMR object discussed in the previous section, the rotation pole of the box-wing shape is difficult for LCI to recover. While the main bus is modeled as a box, which proved possible for LCI to estimate the pole of, the large flat plates used for the solar panels make the attitude more ambiguous. This may be due, in part, to the fact that the version of LCI used in this study implements the original Lommel-Seeliger/Lambert scattering law. While this scattering law may apply to asteroids, it does not capture the specular reflections that will occur from solar panels and antennas. A more appropriate scattering law would be Ashikmin-Shirley or Cook-Torrence, which are analytic BRDF models which capture both diffuse and specular reflections. Implementing these types of scattering laws with LCI may help constrain attitude and shape, but is left for future work.

The LCI shape shown in Fig. 14(b), however, is unique to the box-wing object. LCI captures the box and rotating plate aspects of the box-wing model. Furthermore, even an incorrect pole solution yields a similar shape model as shown in Fig. 16. This is beneficial, in that even if the estimated pole is incorrect, the resulting shape model will indicate that the target object is likely a satellite as opposed to being any other type of object. From that point, other methods (such as MMAE) may be used to further refine the satellite shape, rotation axis, etc.
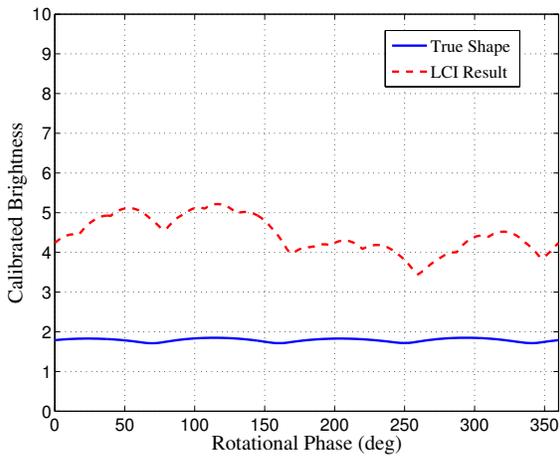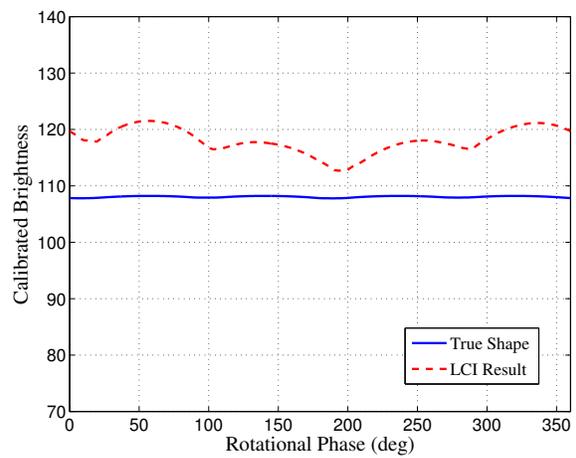
(a) True Shape

(b) LCI Result

Figure 14: Truth and LCI shape models for the box-wing GEO satellite.

(a) $\alpha = 65°$

(b) $\alpha = 15°$

Figure 15: Lightcurve comparisons for two different viewing geometries of the box-wing satellite. The LCI solution is based on the use of the true rotation pole.
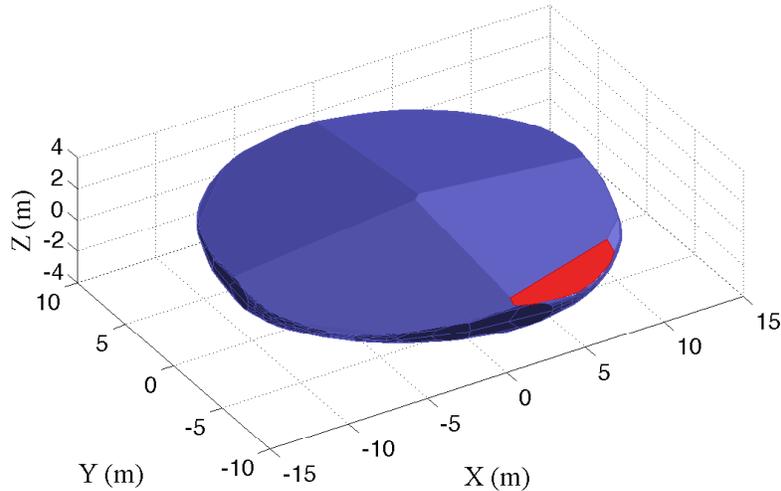
Figure 16: LCI shape solution for the box-wing shape when settled on an incorrect rotation pole.

5. Conclusion and Discussion

In this paper, we analyze the feasibility of using the LCI technique, originally developed to characterize asteroids, for estimating shapes and rotation poles of man-made objects commonly found in Earth orbit. Specifically, we focus on using simulated photometric measurements of GEO objects taken from a space-based sensor in Sun-synchronous orbit. Shape and pole estimation accuracies are given for an ellipsoid, a Centaur upper stage, 1U and 3U CubeSats, a HAMR object, and a box-wing satellite.

The publicly available LCI software suite, developed by M. Kaasalainen and J. Ďurech, is described and used to generate the results presented in this paper. LCI proves to be well suited for estimating shapes that are more naturally convex, such as upper stage rocket bodies and CubeSats. For such objects, the shape and rotation pole are recovered to within 1°, even when given moderate to large errors in the *a priori* pole values.

Plate-like objects and box-wing shapes, however, are shown to be more difficult for LCI to recover. This is not unexpected as the basic form of LCI is built to work with convex shapes. The rotation poles of HAMR objects (i.e., modeled as flat plates) and box-wing satellites cannot be reliably estimated using the current form of LCI implemented here. However, the estimated shapes of these objects are distinctive enough to indicate the type of object being viewed.

Improvements to shape and rotation pole estimation using LCI may be gained by implementing a BRDF model that more accurately describes man-made objects instead of the default used for asteroids and planets. Future work will include adapting the current LCI software to use the Ashikhmin-Shirley BRDF, which is an empirical model that takes both diffuse and specular

reflections into account. It is anticipated that the addition of specular reflections will better retrieve smooth, flat surfaces as well as pole directions. Additionally, this study demonstrates that LCI, even in its current form, may yield a valuable first guess at shape and pole, from which an additional technique, such as MMAE, may be used to further refine the shape, spin, and operational status.

6. Acknowledgment

7. References

[1] Jah, M. K. and Madler, R. A. "Satellite Characterization: Angles and Light Curve Data Fusion for Spacecraft State and Parameter Estimation." "Advanced Maui Optical and Space Surveillance Technologies Conference (AMOS)," Maui, HI, September 11-14 2007.

[2] Wetterer, C. J. "Attitude Estimation from Light Curves." Guidance, Control, and Dynamics, Vol. 32, No. 5, pp. 1648–1651, September-October 2009.

[3] Linares, R., Crassidis, J. L., Jah, M. K., and Kim, H. "Astrometric and Photometric Data Fusion for Resident Space Object Orbit, Attitude, and Shape Determination Via Multiple-Model Adaptive Estimation." "AIAA Guidance, Navigation, and Control Conference," Toronto, Ontario Canada, August 2-5 2010.

[4] Bradley, B. K. and Axelrad, P. "Improved Estimation of Orbits and Physical Properties of Objects in GEO." "Advanced Maui Optical and Space Surveillance Technologies Conference (AMOS)," Maui, HI, September 2013.

[5] Kaasalainen, M. and Torppa, J. "Optimization Methods for Asteroid Lightcurve Inversion: I. Shape Determination." Icarus, Vol. 153, No. 1, pp. 24–36, September 2001.

[6] Kaasalainen, M., Torppa, J., and Muinonen, K. "Optimization Methods for Asteroid Lightcurve Inversion: II. The Complete Inverse Problem." Icarus, Vol. 153, No. 1, pp. 37–51, September 2001.

[7] Kaasalainen, M., Torppa, J., and Piironen, J. "Models of Twenty Asteroids from Photometric Data." Icarus, Vol. 159, pp. 369–395, 2002.

[8] Torppa, J., Kaasalainen, M., Michalowski, T., Kwiatkowski, T., Kryszczyńska, A., Denchev, P., and Kowalski, R. "Shapes and Rotational Properties of Thirty Asteroids from Photometric Data." Icarus, Vol. 164, pp. 346–383, 2003.

[9] Calef, B., Africano, J., Birge, B., Hall, D., and Kervin, P. "Photometric Signature Inversion." "Proceedings of the International Society for Optical Engineering (SPIE)," Vol. 6307. San Diego, CA, September 2006.

[10] Hall, D., Calef, B., Knox, K., Bolden, M., and Kervin, P. "Separating Attitude and Shape Effects for Non-Resolved Objects." "Advanced Maui Optical and Space Surveillance Technologies Conference (AMOS)," Maui, HI, September 2007.

[11] Drummond, J. and Christou, J. "AO Images of Asteroids, Inverting their Lightcurves, and SSA." "Advanced Maui Optical and Space Surveillance Technologies Conference (AMOS)," Maui, HI, September 2008.

[12] Fulcoly, D., Kalamaroff, K., and Chun, F. "Determining Basic Satellite Shape from Photometric Light Curves." Journal of Spacecraft and Rockets, Vol. 49, No. 1, pp. 76–82, January-February 2012.

[13] Wallace, B., Somers, P., and Scott, R. "Determination of Spin Axis Orientation of Geosynchronous Objects Using Space-Based Sensors: An Initial Feasibility Investigation." "Advanced Maui Optical and Space Surveillance Technologies Conference (AMOS)," Maui, HI, September 2010.

[14] Holzinger, M., Alfriend, K., Wetterer, C., Luu, K., Sabol, C., Hamada, K., and Harms, A. "Attitude Estimation for Unresolved Agile Space Objects with Shape Model Uncertainty." "Advanced Maui Optical and Space Surveillance Technologies Conference (AMOS)," Maui, HI, September 2012.

[15] Laurin, D., Hildebrand, A., Cardinal, R., Harvey, W., and Tafazoli, S. "NEOSSat - A Canadian Small Space Telescope for Near Earth Asteroid Detection." Space Telescopes and Instrumentation, 2008.

[16] Maskell, P. and Oram, L. "Sapphire: Canada's Answer to Space-Based Surveillance of Orbital Objects." "AMOS," Maui, HI, September 16-19 2008.

[17] Simms, L., Riot, V., Vries, W. D., Oliver, S., Pertica, A., Bauman, B., Phillion, D., and Nikolaev, S. "Optical Payload for the STARE Mission." "SPIE Defense and Security Conference," LLNL-CONF-474234. Orlando, FL, April 25-29 2011.

[18] Fairbairn, M. B. "Planetary Photometry: The Lommel-Seeliger Law." Journal of the Royal Astronomical Society of Canada, Vol. 99, No. 3, pp. 92–93, June 2005.

[19] Ashikhmin, M. and Shirley, P. "An Anisotropic Phong BRDF Model." Journal of Graphics Tools, Vol. 5, No. 2, pp. 25–32, 2000.

[20] Ashikhmin, M. and Shirley, P. "An Anisotropic Phong Light Reflection Model." Tech. Rep. UUCS-00-014, University of Utah, Salt Lake City, UT, 2000.

[21] Cook, R. L. and Torrance, K. E. "A Reflectance Model for Computer Graphics." "SIGGRAPH Proceedings of the 8th Annual Conference on Computer Graphics and Interactive Techniques," Vol. 15, pp. 307–316. August 1981.

[22] Wetterer, C. J., Linares, R., Crassidis, J. L., Kelecy, T. M., Ziebart, M. K., Jah, M. K., and Cefola, P. J. "Refining Space Object Radiation Pressure Modeling with Bidirectional Reflectance Distribution Functions." Journal of Guidance, Control, and Dynamics, Vol. 37, No. 1, pp. 185–196, January-February 2014.

[23] Papushev, P., Karavaev, Y., and Mishina, M. "Investigations of the Evolution of Optical Chracteristics and Dynamics of Proper Rotation of Uncontrolled Geostationary Artificial Satellites." Advances in Space Research, Vol. 43, pp. 1416–1422, 2009.

[24] Karavaev, Y., Kopyatkevich, R., Mishina, M., Mishin, G., Papushev, P., and Shaburov, P. "The Dynamic Properties of Rotation and Optical Characteristics of Space Debris at Geostationary Orbit." "AAS/AIAA Space Flight Mechanics Meeting," Maui, HI, February 8-12 2004.

[25] Praly, N., Hillion, M., Bonnal, C., Laurent-Varin, J., and Petit, N. "Study on the Eddy Current Damping of the Spin Dynamics of Space Debris from the Ariane Launcher Upper Stages." Acta Astronautica, Vol. 76, pp. 145–153, 2012.

[26] Shirley, P. and Marschner, S. Fundamentals of Computer Graphics. Taylor and Francis Group, LLC, 3rd edn., 2009.

[27] Oltrogge, D. and Leveque, K. "An Evaluation of CubeSat Orbital Decay." "25th Annual AIAA/USU Conference on Small Satallites," SSC11-VII-2. 2011.

[28] Schildknecht, T., Musci, R., Ploner, M., Beutler, G., Kuusela, J., de León Cruz, J., and de Fatima Domínguez Palermo, L. "Optical Observations of Space Debris in GEO and in Highly-Eccentric Orbits." Advances in Space Research, Vol. 34, No. 5, pp. 901–911, 2004.

[29] Schildknecht, T., Vananti, A., Krag, H., and Erd, C. "Physical Characterization of High AMR Debris by Optical Reflectance Spectrometry." "Proceedings of the International Astronautical Congress 2010," A6.1.7. Prague, Czech Republic, September 2010.

[30] Früh, C. and Schildknecht, T. "Variation of the Area-to-Mass Ratio of High Area-to-Mass Ratio Space Debris Objects." Monthly Notes of the Royal Astronomical Society, Vol. 419, pp. 3521–3528, 2012.

[31] Früh, C., Kelecy, T., and Jah, M. "Coupled Orbit-Attitude Dynamics of High Area-to-Mass Ratio (HAMR) Objects: Influence of Solar Radiation Pressure, Earth's Shadow and the Visibility in Light Curves." Celestial Mechanics and Dynamical Astronomy, Vol. 117, pp. 385–404, 2013.